XMapTools: A MATLAB©-based program for electron microprobe X-ray image processing and geothermobarometry

Pierre Lanari, Olivier Vidal, Vincent de Andrade, Benoît Dubacq, Eric Lewin, Eugene G. Grosch, Stéphane Schwartz

XMapTools: a MATLAB©-based program for electron microprobe X-ray image processing and geothermobarometry

Pierre Lanari[a,b,*], *Olivier Vidal*[b], *Vincent De Andrade*[c], *Benoît Dubacq*[d,e,f], *Eric Lewin*[b], *Eugene G. Grosch*[g] *and Stéphane Schwartz*[b]

[a] Institute of Geology, University of Bern, Baltzestrasse 1+3, CH-3012 Bern, Switzerland.

[b] ISTerre, Université de Grenoble I, CNRS, 1381 rue de la Piscine. 38041 Grenoble, France.

[c] NSLS II, Brookhaven National Laboratory, SRX beamline, Bldg 817 Renaissance Road, Upton, New York 11973, USA.

[d] Department of Earth Sciences, University of Cambridge, Downing Street, Cambridge CB2 3EQ, UK

[e] UPMC Univ. Paris 06, ISTEP, UMR 7193; F-75005 Paris, France

[f] CNRS, ISTEP, UMR 7193; F-75005 Paris, France.

[g] Department of Earth Science and Centre for Geobiology, University of Bergen, Allegaten 41, N-5007, Bergen, Norway.

*Corresponding author. Fax +41 031 631 48 43.

E-mail address: pierre.lanari@geo.unibe.ch (P. Lanari)

Computers & Geosciences, 62 (2014) 227-240

Abstract

XMapTools is a *MATLAB*©-based graphical user interface program for electron microprobe X-ray image processing, which can be used to estimate the pressure-temperature conditions of crystallization of minerals in metamorphic rocks. This program (available online at http://www.xmaptools.com) provides a method to standardize raw electron microprobe data and includes functions to calculate the oxide weight percent compositions for various minerals. A set of external functions is provided to calculate structural formulae from the standardized analyses as well as to estimate pressure-temperature conditions of crystallization, using empirical and semi-empirical thermobarometers from the literature. Two graphical user interface modules, *Chem2D* and *Triplot3D*, are used to plot mineral compositions into binary and ternary diagrams. As an example, the software is used to study a high-pressure Himalayan eclogite sample from the Stak massif in Pakistan. The high-pressure paragenesis consisting of omphacite and garnet has been retrogressed to a symplectitic assemblage of amphibole, plagioclase and clinopyroxene. Mineral compositions corresponding to ~165 000 analyses yield estimates for the eclogitic pressure-temperature retrograde path from 25 kbar to 9 kbar. Corresponding pressure-temperature maps were plotted and used to interpret the link between the equilibrium conditions of crystallization and the symplectitic microstructures. This example illustrates the usefulness of *XMapTools* for studying variations of the chemical composition of minerals and for retrieving information on metamorphic conditions on a microscale, towards computation of continuous pressure-temperature-and relative time path in zoned metamorphic minerals not affected by post-crystallization diffusion.

Keywords: *XMapTools* program; X-ray chemical imaging; quantitative micro-mapping; *PT*-maps

1. Introduction

Our understanding of the geodynamics and processes in orogens, subduction zones and the lower crust relies on estimations of the pressure-temperature (*P-T*) conditions of crystallization of mineral assemblages. Deriving reliable pressure and temperature information from a rock is critical to our knowledge of the thermal structure of the crust, whose variations can be recorded through time within individual samples via consecutive partial re-equilibration events. Thermobarometric tools such as multi-equilibrium thermobarometry (e.g. Berman, 1991), pseudosections (e.g. Holland and Powell, 1998; 2011) and empirical thermometers (e.g. Cathelineau and Nieva, 1985) provide these estimates from the nature and composition of minerals, even for high-variance assemblages (Vidal and Parra, 2000). To shed light on the recrystallization history of metamorphic rocks, chemical compositions of the minerals are required. This is commonly achieved using point mode analyses obtained with an electron probe microanalyser (EPMA). The use of X-ray images allows to identify the relationships between microstructures, variations of composition and variations of *P-T* conditions of crystallization (e.g. Vidal et al., 2006). Since the first X-ray "dot maps" compositional image (Cosslett and Duncumb 1956), this technique has been developed (see Friel and Lyman 2006 for a review) using both energy-dispersive and wavelength dispersive X-ray spectrometers (EDS and WDS). For instance, previous work has used X-ray images for classification and modal analysis (Launeau et al.,

1994; Bonnet, 1998; Cossio et al., 2002; Prêt et al., 2010) and to reconstruct *P-T* paths (Kohn and Spear, 2000; De Andrade et al., 2006; Muñoz et al., 2006; Vidal et al., 2006; Yamato et al., 2007; Ganne et al., 2012; Fiannacca et al., 2012; Lanari et al., 2012; Plunder et al., 2012; Pourteau et al., 2013; Lanari et al., 2013). Quantitative electron microprobe analyses require an analytical standardization of the number of collected photons (X-ray intensity). The acquisition time for standardized point analysis for eight major elements (e.g. Si, Al, Mn, Mg, Fe, Na, Ca, K) under classical conditions (typically 10nA, 15keV, 40s) averages around two minutes. This approach is therefore difficult to apply to chemical mapping, where samples are typically heterogeneous on a ~10μm scale and maps typically contain about 150 000 pixels, that would correspond to ~200 days of measurements. X-ray maps for quantitative mapping can be obtained within a reasonable time frame by using a higher current intensity and a lower counting time (100nA, 15 KeV, 100-300ms, see De Andrade et al., 2006). In order to transform the X-ray intensities into calibrated weight percentages, Clarke et al. (2001) used a Bence-Albee approach (Bence and Albee, 1968), which has been later implemented in the program XRMapAnal (Tinkham and Ghent, 2005). However, the precision of this standardization procedure is subject to caution, because it can result in unreliable compositions for some geologically important phases (e.g. quartz, muscovite, plagioclase and garnet, compositions listed in the table 3 of Tinkham and Ghent, 2005). De Andrade et al. (2006) showed that standardization of X-ray intensities using point analyses as internal standards (Castaing, 1951) provides more reliable results.

In the present contribution, we present a *MATLAB*© -based Graphical User Interface (GUI) program named *XMapTools* that can be used to: (1) classify mineral phases in the sample, (2) convert X-ray intensities into calibrated weight percentages using

101 Castaing's approach, (3) calculate the structural formulae of the identified minerals,
102 (4) plot minerals compositions using various chemical diagrams, and (5) calculate *P-T*
103 conditions of equilibration using various empirical and semi-empirical
104 thermobarometers. An example of application of the program to a retrogressed
105 eclogite is presented below.
106
107 **2. Description of the program**
108 The *XMapTools* program (available at http://www.xmaptools.com) can be run with a
109 *MATLAB*© version 7.5 release R2007b or later. It uses a graphical interface named
110 *XMapTools.fig* (Fig. 1) built using the *MATLAB*© Graphical User Interface
111 Development Environment (GUIDE) tool. Each of the GUI components dragged with
112 the GUIDE is associated with a callback function in the program file *XMapTools.p*,
113 corresponding to a content-obscured version (encrypted executable).
114 The program is structured into three parts: *Xray*, *Quanti* and *Results* (Fig. 2)
115 corresponding to three different steps of the mapping process. The first step (Xray
116 column in Fig. 2), starts by loading the map. From statistical analysis of their
117 composition, pixels are grouped within mineral phases and possibly fractures or
118 voids, and corresponding masks are created. The user then identifies the nature of the
119 various groups. This steps ends with the standardization stage. In the second step,
120 (Quanti column in Fig. 2), standardized maps are turned into maps of structural
121 formulae and into *P-T* maps. The last step (Results column in Fig. 2), allows the user
122 to produce binary and ternary chemical diagrams with the *Chem2D* and *TriPlot3D*
123 modules. All the functions used in these different stages are detailed below.
124
125 **2.1 Raw data treatment (Xray)**

Two types of datasets can be uploaded into *XMapTools*, namely the raw X-ray data in photon counts per pixel (matrixes corresponding to the number of collected photons per analyzed element per pixel) and the point analyses used as internal standards.

With both *Cameca*© and *Jeol*© EPMA, the raw data of chemical maps can be exported in *ASCII* format text files such as **.txt* file. Typically, one file is created for each measured element, and contains header lines reporting information about analytical conditions and coordinates of the selected area, followed by a matrix of X-ray intensity data (see Appendix 1). After removal of the header lines by the user, the loading function of XMapTools reads the input files and creates X-ray intensity images. This function includes dead-time correction, where the time interval after the arrival of a pulse during which the spectrometer is unresponsive to further pulses (Reed 2005) is accounted for, and transforms the measured counting rates into true rates.

Point analyses, their coordinates and the map coordinates are the other required inputs to the standardization step. Usually, the point analyses are made along different transects at high angles to (mineral grain boundaries includes 'each other') mineral grain boundaries to capture the total extent of the minerals heterogeneity. Experience has shown that a minimum of 20 point analyses encompassing most of the chemical heterogeneity of each mineral phases in the selected area of the sample is necessary to reach optimum precision. The standard loading function reads a series of point analyses. The locations of the point analyses must be carefully reported from stage coordinates corrected for mechanical backlash and are then projected on the map with the EMPA map coordinate system. The user can compare the X-ray intensities along the profiles measured by point analyses to those of the map, which is useful to detect problems of location of profiles on the map, for example due to drifting of the sample

151 stage during analysis or to a projection problem. The point analyses showing outlying
152 or unwanted compositions such as mixtures of fine minerals, inclusions, or grain
153 boundaries must be deleted before the standardization.
154
155 **2.1.1 Classification: mask creating function**
156 This function creates masks corresponding to entities identified in the map (e.g.
157 mineral, mineral boundaries, fractures), where each mask is a matrix of logical
158 numbers indexed on the coordinates of the composition map: the value of 1 is
159 attributed to the pixels belonging to a given mineral phase, and 0 to the other pixels.
160 This function allocates each individual pixel to one of the minerals phases. The mask
161 creating function uses the statistical analysis method K-means clustering to distribute
162 the pixels into groups of similar compositions. K-means identifies clusters and
163 allocates pixels to these clusters by minimization of the distance in compositional
164 space between the pixels and the gravity centre of each cluster (Saporta 1990).
165 The user selects one pixel of each phase on the chemical map as needed by the mask
166 creating function for initial guess. The compositions of these pixels are used as
167 starting cluster centroids. In an iterative loop, each pixel is assigned to the nearest
168 cluster and the centroids are recalculated until the sum of point-to-centroid
169 distancesover all clusters is minimized (Seber, 1984; Spath, 1985). Two approaches
170 are available in *XMapTools*: the 'normalized' and the 'classical' approaches. Both of
171 them use a K-means clustering approach, but with different X-ray intensities inputs.
172 In the 'normalized' function, X-ray intensities of each element are normalized to their
173 mean values, with the result that all elements have the same weight and only the
174 variances are compared. In contrast, the X-ray intensities of each element in the
175 'classical' method depend on the absolute concentration in each element. This

176 ‘classical’ method is therefore more appropriate for elements present in high
177 concentration. Different masks may be derived using both methods, depending on the
178 magnitude of the differences between the compositions of the phases. An example is
179 shown in section 3.2. Other approaches for the classification of different mineral
180 phases can be found in the PetroMod program (Cossio et al., 2002). Here the K-means
181 algorithm was chosen for its straightforwardness and efficiency.
182
183 **2.1.2 Standardization function**
184 The analytical standardization consists in converting the measured X-ray intensities
185 into oxide weight percent concentrations using standards (Reed, 2005). The
186 standardization function performs this transformation for each mask where
187 quantitative information is available from point analysis or using user-defined
188 concentrations. The standardization of pixels requires calibration curves describing
189 how X-ray intensities change with concentration (Castaing, 1951). One calibration
190 curve is calculated for each element in each phase from the intensity versus
191 concentration relations constrained with point analyses. The calibration curves for Si
192 in the different phases of the studied sample are shown in Figure 3. For each mineral,
193 the calibration curve is a straight line between the origin (0 intensity and
194 concentration) and the central point of the cluster of the point analyses.
195 The standardization can be performed using one of the three methods available in
196 *XMapTools*. The first method ‘Auto (median approach)’ is fully automatic, and the
197 cluster centroids are the median values separating the higher half from the lower half
198 of the data. The ‘Manual’ approach allows the user to define the center of the clusters
199 and therefore the calibration curve. The last method ‘Manual (homogeneous phase)’ is
200 adapted to minerals assumed to be homogeneous such as might be the case for quartz.

The calibration curve is then defined as the mean value of X-ray intensity for the selected mineral and the user enters the corresponding concentration, e.g. 100% for SiO_2 in the case of quartz.

2.2 Calculations from quantified data (Quanti)

Once the masks have been defined and element concentrations have been estimated, structural formulae may be calculated and equilibrium conditions derived using external functions (see below). Users can add new thermobarometry or structural formula functions. The file 'List-thermometers.txt' lists all information about these external functions (i.e. category, name, input and output variables) that are stored into the folder 'Functions'. All these functions are *MATLAB*© script m-files that can be read and edited.

2.2.1 Structural formulae functions

Several structural formulae and atom site allocations models from the literature are implemented in *XMapTools* (Table 1). A general function is also available to calculate a structural formula normalized to a given number of oxygen atoms. This additional function is used to compute the number of moles of elements per formula unit (p.f.u.) for each pixel assuming that the total sums up to 100%.

2.2.2 Thermobarometry functions

XMapTools includes a large selection of thermobarometry functions based on empirical and semi-empirical calibrations. These methods are distributed into two groups: exchange reactions for thermometry (Table 2) and thermobarometer functions (Table 3).

In exchange reactions, cations such as Fe^{2+} and Mg^{2+} are swapped between two minerals (e.g. Spear, 1995). *P-T* conditions of equilibrium may be derived from the cations partition between the two phases (e.g., Ravna, 2000a for garnet-clinopyroxene). *XMapTools* generates an image with the oxide weight percent compositions of the two minerals and allows the user to select pairs of pixels (spot mode) or pairs of groups of pixels (area mode).

In the spot mode, the selected compositions are used to estimate the equilibrium conditions. In the area mode, all the possible pairs of pixels are used to calculate an average equilibrium condition with associated uncertainty. This mode allows to propagate the effect of composition variation in any phase through the whole thermobarometer calculation.

For exchange reactions, *T* is usually estimated for a given pressure. If the minerals exhibit metamorphic zoning preserving paleo-equilibrium conditions, and if the zoning pattern is not due to post-crystallization diffusion, the variations of *T* conditions can be investigated using exchange reactions. A set of mineral pairs selected between the core and the rim of two minerals provides a trend for the evolution of the temperature conditions. This approach is essentially the same as commonly used with point analyses.

The thermobarometry functions provide information on the *T* and/or *P* of mineral crystallization for each pixel of the map, which can be turned into *P*, *T*, or *P and T* maps. Both *P* and *T* conditions are derived from only one mineral composition (one pixel) with fixed variables such as other mineral composition, or *P* or *T*. Methods are listed in Table 3 in three groups: (1) thermometers, (2) barometers, and (3) thermobarometers where *P-T* conditions are derived from at least two reactions (one *T-dependent* and one *P-dependent*) within a given mineral assemblage. This is done

using groups of pixel compositions and assuming equilibrium between the groups.

The use of thermobarometry functions should be restrained to cases where the relevant saturating assemblages are present in the studied sample. The functions implemented in XMapTools do not check the presence of such assemblages because some minerals may be outside the mapped area. This is then the responsibility of the user to decide whether the functions can be applied to the studied sample.

2.3 Chemical plots

The mineral compositions or end-member proportions can be plotted as maps or into chemical diagrams such as binary diagrams (Fig. 4a) using the *Chem2D* module, or ternary diagrams (Fig. 5a) using the *Triplot3D* module. Both modules have a graphical interface in which the user can select the plotted variables and manage the diagram axes. A density plot function is also available to contour the analyzed variables for density, which is useful when a large number of points is plotted as is the case when working with maps (see examples in Fig. 4b and 5b). This function displays a density map using the mineral composition data and grid spacing defined by the user for density counting. The unit of the output of the density map is a number of analyses per surface unit of the grid on the graph, which has the dimension of the x axis multiplied to the y axis.

Two selection functions, namely ‘identify pixels’ and ‘multi-groups’, may be used to select ranges of composition (rectangles) in the diagrams, as well as to identify the selected pixels on the corresponding map (Fig. 4c and Fig. 5c) and to calculate modal abundances.

Several functions may be used to create masks from user-defined chemical groups within a phase. These masks are either built from manual selections (with the tools

276 “identify pixel” and “multi-groups”) or automatically using a K-means clustering
277 approach. The mask variable can be exported into ASCII format (*.txt file) and used
278 in the *Quanti* stage to export the average oxide composition corresponding to a
279 selection of pixels.
280
281 **2.4 Other functions**
282 All the results can be saved and previously saved projects can be loaded at any time
283 using the functions ‘save’, ‘save as’ and ‘load’. The save functions store the data in a
284 MATLAB© formatted binary file MAT-file (with .mat extension).
285 Functions in the ‘figure’ window are dedicated to the management of the color bar
286 such as setting the minimum and maximum values, the auto and reset buttons, and the
287 phase separator button (PhaseSep in Fig. 1). The user can also export the main figure
288 in usual image formats.
289 Functions in the ‘sampling’ window are used to select a subset of the data into the
290 main displayed image. These functions are available for any image (X-ray raw
291 measurement, map of oxide compositions, structural formulae, equilibrium conditions
292 maps). The selected data may be individual pixels, arrays or areas of pixels. This tool
293 can be used for example to draw the composition variations of a mineral grain along a
294 transect.
295
296 **3. Tests and evaluation**
297 Generating structural formulae and *P-T* maps from microprobe analysis is of interest
298 for petrology and geodynamics studies. In this section, we present an example of the
299 use of *XMapTools* on a metamorphic rock sample. Compositional maps were acquired
300 on an eclogite sample from the Stak area, a high pressure (HP) continental massifs in

NW Himalaya (Guillot et al., 2008; Lanari et al., 2013). This sample contains a well-preserved eclogitic assemblage consisting of garnet and omphacite, which formed during continental subduction. Omphacite was subsequently retrogressed to a Na-poorer clinopyroxene + plagioclase + amphibole symplectite. The final metamorphic event is recorded in the sample as a foliation comprising large crystals of amphibole developed as a result of deformation and syntectonic hydration under mid-upper crustal conditions (Lanari et al., 2013).

3.1 Data acquisition

An area of 0.348 mm^2 (520μm × 670μm) located in a symplectite zone and containing garnet, clinopyroxene, amphibole, plagioclase, Ti- and Fe-oxides was mapped at the Institute of Earth and Environmental Science, University of Potsdam, using a JEOL JXA-8200 EMPA. Mapping conditions were 15 keV accelerating voltage and 100 nA beam current, beam diameter smaller than 1 μm, 200 ms dwell time and 1 μm step size (i.e. pixel size). X-ray intensities for Si, Ti, Al, Fe, Mg, Mn, Ca, Na and K were measured in two passes.

3.2 Classification

An image of the mineral phases created using the 'mask creating function' (see §2.1) is shown in Figure 6a. The two methods for the mask creating function (classical and normalized) were tested and lead to similar estimates of the mineral modal proportions except for garnet (Table. 4). The difference for garnet is due to the erroneous allocation of the contour pixels around amphibole to the garnet mask when using the classical approach. This artefact may be corrected by creating an additional mask corresponding to the borders of the mineral or by using the normalized method.

326 Additional differences between the ‘normalized’ and ‘classical’ approaches are shown
327 in Figure 6b for a part of the map (dashed square in Fig. 6a). For instance, zone 1 in
328 Fig. 6b shows that omphacite is identified in the core of clinopyroxene using the
329 ‘normalized’ method only. This is due to the normalization procedure and originates
330 from the small chemical differences between omphacite and clinopyroxene in their
331 Na- and Mg-contents. These differences are not detected with the ‘classical’ method,
332 which allocates more pixels to the clinopyroxene mask. The other examples (2 and 3
333 in Fig. 6) show that in some cases, the opposite effect is observed when variations
334 occur in only one highly concentrated element, keeping effects of the variations in
335 low-concentrated elements to a minimum. From this, we conclude that the two
336 methods should be tested and we recommend to check the difference between the two
337 results and to compute different mask-files with different number of phases (including
338 the fractures and/or mineral boundaries).
339
340 **3.4 Test of the standardization**
341 Analytical standardization of the X-ray images was performed using the
342 ‘standardization function’ (see §4.1) with the ‘Auto (median approach)’ method.
343 Calibration curves (see §3.1 and graphical representation in Fig. 3) were calculated
344 for clinopyroxene, garnet, amphibole and plagioclase.
345 The quality and accuracy of the standardization can be investigated using the function
346 ‘Test of standardization’. This function plots the composition difference between
347 point analyses and the standardized composition on the same location on the maps. As
348 an example, the results for the standardization of garnet are reported in Fig. 8, which
349 shows that the pixel compositions derived from the standardized maps are in good
350 agreement, within analytical uncertainties, with the corresponding point analyses for

elements showing homogeneous compositions such as SiO_2, Al_2O_3, FeO (Fig. 8a, 8b and 8c) and heterogeneous compositions due to zoning such as CaO, MgO and MnO (Fig. 8d, 8e and 8f). In contrast, the point analyses of low concentration elements TiO_2 and K_2O show trends not recorded in the standardized maps (Fig. 8g and 8h), indicating that the concentrations of TiO_2 and K_2O mapped in garnet are not reliable, because they are close to the detection limits for the used mapping analytical conditions.

3.5 Structural formulae and chemical study

Clinopyroxene structural formulae were calculated on a 6 oxygen-basis by distributing elements on tetrahedral (T1) and octahedral (M1, M2) sites. End-members proportions of jadeite, diopside, hedenbergite, acmite and Ca-tschermak (Table 1) were estimated according to the atom site allocation model of Spear (1995) and Warren and Waters (2006). The amphiboles structural formulae were calculated on a 23 oxygen-basis and elements were distributed on tetrahedral (T1, T2), octahedral (M2, M13, M4), and 10 to 12-fold coordinated (A) sites. End-members proportions of glaucophane, tremolite, tschermakite, pargasite, cumingtonite (Table 1) were calculated according to the atom site allocation model of Dale et al. (2000; 2005). Structural formulae for garnet and plagioclase were respectively calculated on a 12 and 8 oxygen-basis following classical atom-site allocation models (Table 1). Structural formulae maps highlight the relationship between atom-site composition and microstructures. The two chemical modules *Chem2D* and *Triplot3D* were used to investigate the variations of clinopyroxene structural formulae (i.e. varying end-member proportions). In Figure 4a, Na-rich clinopyroxene compositions were selected (red dots) using the 'identify pixel' tool (§2.3) in the Na vs. Mg diagram. The

pixels belonging to the selected composition range are plotted in red on the map (Fig. 4c). These Na-rich clinopyroxene compositions are omphacitic and make up to ~25% of the total clinopyroxene pixels. Then, clinopyroxene compositions were divided into three groups using the 'multi-groups' tool within the jadeite-diopside-hedenbergite ternary diagram (groups 1, 2 and 3 in Fig. 5a). The pixels belonging to the three composition ranges are plotted on the map with corresponding colors (Fig. 5c). The clinopyroxene compositions into the symplectite have lower Na contents, corresponding to lower jadeite contents. Clinopyroxene-amphibole-plagioclase symplectites are known to nucleate on grain boundaries between two omphacite grains and to grow into the grain on one side, when the rock is sufficiently out of equilibrium to nucleate the product (Joanny et al., 1991; Waters, 2002, 2003). In the mapped area (Fig. 7), Na-rich clinopyroxene previously identified as omphacite shows high Na contents (up to 0.4 p.f.u, zone 1 in Fig. 7). This primary omphacite (width > 100μm) is destabilized into a first symplectite containing Na-poorer clinopyroxene, plagioclase and amphibole. Clinopyroxene in this first symplectite (zone 2 in Fig. 7) crystallizes as broad lamellae (30-40μm width) preserving the original shape of omphacite, but with a lower Na-content (0.35 to 0.28 p.f.u.) than the original omphacite grains. A second symplectite with the same minerals is observed in zone 3 of figure 7, which shows smaller-size clinopyroxene lamellae (10-20μm width) and Na-content (0.28 to 0.18 p.f.u.). Clinopyroxene lamellae are even smaller in the last symplectite (width < 10μm) and also have lower Na-content (<15 p.f.u.).

3.6 Precision and resolution

In the previous section, maps of structural formulae highlight variations in the clinopyroxene composition according to the symplectite microstructures. Na-content

401 in clinopyroxene decreases with decreasing size of the symplectite (i.e. with time).
402 The clinopyroxene solid solution includes jadeite while diopside hedenbergite and Ca-
403 tschermak are calcic end-members. As the multiplicity of the M2 site is one and
404 $XFe^{3+} = 0$ (corresponding to $X_{acmite} = 0$), the jadeite proportion is equal to the Na-
405 content in clinopyroxene. Estimating the uncertainties associated with the
406 compositional values of the structural formulae is needed before discussing the
407 implications linked to the chemical zoning.
408 The precision of the electron microprobe measurement with our experimental protocol
409 can be estimated using a Poisson law (De Andrade et al., 2006):

410 $$p = \frac{2}{\sqrt{n}} \quad (1)$$

411 with p the precision (in % at 2σ), and n the number of recorded counts. The mean
412 intensities and precision measurements for each element (Si, Ti, Al, Fe, Mg, Ca, Na,
413 K) of clinopyroxene pixels are listed in Table 4. The precision measurements range
414 from 1.8% for Si to 20% for Ti. Uncertainties in the structural formula originating
415 from analytical errors were estimated using a Monte Carlo simulation where a total of
416 100 000 random clinopyroxene compositions were computed with a normal
417 distribution around the mean intensity compositions (Table 4) within 2σ of the
418 measured precisions. The standardization procedure was carried out for all the
419 compositions using the calibration curves estimated above. The average oxide
420 concentrations structural formulae and the associated standard deviations are listed in
421 Table 4. The average Na-content is estimated at 0.28 ± 0.03 p.f.u., which indicates
422 that the compositional variations identified above (ranging from 0.41 to 0.13) are
423 significant. It is emphasized that the uncertainties reported here are valid for the
424 present EPMA settings and range of clinopyroxene composition, and can be decreased
425 by increasing the dwell time.

426

427 **3.7 Combined *P* and *T* functions: *P-T* maps of Cpx**

428 *P-T* maps were built using combined *P* and *T* functions available in *XMapTools*
429 (description in §4.2 and list in Table 2). At the thin section scale, two assemblages
430 involving clinopyroxene are in equilibrium: the HP assemblage made of garnet,
431 omphacite and phengite (as inclusions in garnet, not present in the mapped area) and
432 the retrogressed assemblage represented by the clinopyroxene-plagioclase-amphibole
433 symplectite. These two parageneses were treated separately.

434 For the HP assemblage, *P-T* conditions for clinopyroxene pixels were estimated using
435 the *XMapTools* function 'Cpx-P-T Rav (Omp-Gar-Phg)'. *P* was estimated using the
436 garnet, omphacite and phengite geobarometer of Waters and Martin (1993) and
437 Waters (1996). *T* was estimated using the garnet and omphacite geothermometer of
438 Ravna (2000a). The function estimates first T_1 at a given *P* (P_{input}), and recalculates
439 T_{n+1} and P_{n+1} until convergence (respectively 5°C and 0.1 kbar) between T_n and T_{n+1}
440 and P_n and P_{n+1}. As the compositions of garnet show a slight zoning (Alm_{48} $Prp_{32–33}$
441 $Grs_{17–19}$ Sps_1), two average garnet compositions were defined, one for the core and
442 one for the rim (Lanari et al., 2013). In both groups, garnet compositions are
443 homogeneous within errors. Each pixel of omphacite was assumed in equilibrium
444 with one garnet average composition (core-core, rim-rim). Then, *P-T* estimates were
445 calculated for all omphacite compositions.

446 For the symplectite, *T* was first estimated using the edenite-richterite calibration
447 (Holland and Blundy, 1994) with the composition of amphibole pixels for a fixed
448 composition of plagioclase (function 'Amp-T, Holland and Blundy 1994a').
449 Crystallization *T* for amphibole were found to vary from 680±6°C in contact with
450 $Jd_{30\%}$ clinopyroxene to 640±8°C in contact with $Jd_{10\%}$ clinopyroxene. This

451 relationship was used to calculate the *T* of clinopyroxene. *P* for clinopyroxene
452 crystallization were subsequently calculated using the calibration of Waters (2003) for
453 the equilibrium reaction: jad + trem = alb + ed.
454 About 165 000 *P-T* calculations (one for each Cpx pixels) have been obtained and the
455 results have been plotted into binary diagrams (Fig. 9a and 9b) using the module
456 Chem2D, and into *P* and *T* maps (Fig. 9c and Fig. 9d). The density *P-T* diagram
457 option (Fig. 9b) plotted using the Chem2D module shows that the apparent deviation
458 in *P* is composed of a small proportion of points (< 1%). In contrast, the density
459 diagram shows a significant trend for *T* and *P* corresponding to the prograde evolution
460 from 650°C to 750°C and from 24 kbar to 25 kbar. This increase in *T* and the slight
461 increase of *P* along the prograde path is confirmed by the spatial distribution of the
462 obtained *T* and *P* when plotted on a map: omphacite grains show high *P* at ~25kbar,
463 and are zoned in *T* from 650°C in the old grain cores to 750°C in the old grain rims.
464 Clinopyroxene in the symplectite shows a different trend with a decrease of both *P*
465 and *T* with the decreasing size of the intergrowths (Fig. 9). This interpretation on the
466 preservation of P and T in symplectite during the exhumation is in good agreement
467 with the reported high cooling rates (Guillot et al., 2009). This example typifies the
468 importance of the mapping approach, which allows to test for relationships between
469 *P-T* conditions and the textural information from metamorphic microstructures.
470
471 **4. Concluding remarks**
472 This paper describes XMapTools, a MATLAB©-based GUI program to quantify raw
473 X-ray electron microprobe data using internal standards, plot chemical diagrams and
474 calculate *P-T* conditions of crystallization for metamorphic parageneses. The
475 XMapTools program includes 15 user-friendly main functions for the different steps

476 to the procedure, from the loading of the raw data to calculating *P-T* maps, and two
477 external modules *Chem2D* and *TriPlot3D* with independent graphical user interfaces
478 to plot chemical diagrams. Beside the treatment of compositional maps, XMapTools
479 offers the possibility of estimating thermobarometric conditions, which can be linked
480 to the observed deformation features. For the study of metamorphic and magmatic
481 rocks, a set of external functions specific to geothermobarometry is also included.
482 This set comprises a range of structural formulae functions for usual rock-forming
483 silicate minerals as well as empirical and semi-empirical geothermobarometers from
484 the literature. Application of XMapTools to an eclogite sample shows that the
485 accuracy of the mapped minerals composition is good enough to discuss the
486 compositional-structural-*P-T* relationships based from Na distribution in
487 clinopyroxene. A strong link between metamorphic textures and composition has
488 been found, and the retrieved *P-T* information gives a detailed reconstruction of the
489 metamorphic history of the sample.
490 A more detailed thermobarometric study can be made using independent programs
491 such as e.g. Theriak-Domino (de Capitani and Petrakakis 2010) or Tweeq (Berman,
492 2007) with the whole range of mineral compositions derived from XMapTools, which
493 can be easily exported to the required formats. Moreover, an interesting feature of
494 XMapTools is the possibility to calculating local bulk rock compositions from
495 selected parts of the 2D maps. Such compositions can be used to calculate the stable
496 mineral assemblages, compositions and abundance by free energy minimizing (e.g.
497 Powell, 2008), and to compare them with the observed features. This approach,
498 illustrated in Lanari et al. (2013) for the example discussed in the present
499 contribution, can provide valuable information on the degree of achievement of
500 thermodynamic equilibrium, the link between deformation and reequilibration, and

possibly the extend of mass transfer controlled by deformation. Future release of XMapTools will incorporate energy minimizing and multi-equilibrium modules to facilitate advanced thermobarometric studies.

5. Acknowledgements

Authors acknowledge A. Pourteau for his help with the EPMA analyses, N. Riel, C. Martin, F. Guillot, B. Gardonio, F. Bernier, M. Engi, M. Muñoz, K. Malamoud, A. Robert, J. de Sigoyer, P. Agard and S. Guillot for help, comments, data and/or collaborations in order to test the different versions of XMapTools. Authors thank G. Ortolano, D. Waters and one anonymous reviewers for constructive comments and Jef Caers for editorial handling. This work was supported by the French ANR project "ERD-Alps".

6. References

Ai, Y., 1994. A revision of the garnet-clinopyroxene Fe^{2+}-Mg exchange geothermometer. Contrib. Min. Petrol. 115(4), 467–473

Anderson, J.L., Smith, D.R., 1995. The effects of temperature and f_{02} on the Al-in-hornblende barometer. Am. Min. 80, 549–559.

Bence, A.E. and Albee, A.E., 1968. Empirical correction factors for the electron microanalysis of silicates and oxides. Journal of Geology. 76, 382-403.

Berman, R.G., 1991. Thermobarometry using multi-equilibrium calculations: a new technique, with petrological applications. Can. Min. 29, 833–855.

Berman R. G. 2007. WinTWQ (version 2.3) a software package for performing internally-consistent thermobarometric calculations. Geological Survey of Canada pp. 41.

Blundy, J.D., Holland, T.J.B., 1990. Calcic amphibole equilibria and a new amphibole-plagioclase geothermometer. Contrib. Min. Petrol. 104, 208–224.

Bonnet, N. (1998). Multivariate statistical methods for the analysis of microscope image series: applications in material science. Journal of Microscopy. 190, 2-18.

Castaing, R., 1951. Application des sondes electronique a une methode d'analyse ponctuelle chimique et cristallographique. Université de Paris (publication ONERA), Paris.

Cathelineau, M., 1988. Cation site occupancy in chlorites and illites as function of temperature. Clay Min. 23, 471–485.

Cathelineau, M., Nieva, D., 1985. A chlorite solid solution geothermometer the Los Azufres (Mexico)

534 geothermal system. Contrib. Min. Petrol. 91, 235–244.

535 Clarke, G.L., Daczko, N.R. and Nockolds, C. 2001. A method for applying matrix corrections to X-ray
536 intensity maps using the Bence-Albee algorithm and Matlab. J. Metam. Geol. 19, 653-644.

537 Coggon, R., Holland, T., 2002. Mixing properties of phengitic micas and revised garnet-phengite
538 thermobarometers. J. Metam. Geol. 20, 683–696.

539 Cossio, R., Borghi, A., Ruffini, R. (2002) Quantitative modal determination of geological samples
540 based on X-ray multielemental map acquisition. Microsc. Microanal. 8, 139-149.

541 Cosslett, V.E. and Duncumb, P. (1956). Microanalysis by a flying-spot X-ray method. Nature. 177,
542 1172-1173.

543 Creighton, S., 2009. A semi-empirical manganese-in-garnet single crystal thermometer. Lithos 112,
544 177–182.

545 Dahl, P.S., 1980. The thermal-compositional dependence of Fe^{2+}-Mg distributions between coexisting
546 garnet and pyroxene: applications to geothermometry. Am. Min. 65(85), 866.

547 Dale, J., Holland, T., Powell, R., 2000. Hornblende–garnet–plagioclase thermobarometry: a natural
548 assemblage calibration of the thermodynamics of hornblende. Contrib. Min. Petrol. 140, 353–
549 362.

550 Dale, J., Powell, R., White, R., Elmer, F., Holland, J., 2005. A thermodynamic model for Ca–Na
551 clinoamphiboles in Na2O–CaO–FeO–MgO–Al2O3–SiO2–H2O–O for petrological calculations.
552 J. Metam. Geol. 23, 771–791.

553 De Andrade, V., Vidal, O., Lewin, E., O'Brien, P., Agard, P., 2006. Quantification of electron
554 microprobe compositional maps of rock thin sections: an optimized method and examples. J.
555 Metam. Geol. 24, 655–668.

556 de Capitani C. and Petrakakis K. (2010): The computation of equilibrium assemblage diagrams with
557 Theriak/Domino software. Am. Min. 95, 1006-1016

558 Dickenson, M., Hewitt, D., 1986. A garnet-chlorite geothermometer. Geol. Soc. Am. Abstr. 18, 584.

559 Dubacq, B., Vidal, O., Andrade, V., 2010. Dehydration of dioctahedral aluminous phyllosilicates:
560 thermodynamic modelling and implications for thermobarometric estimates. Contrib. Min.
561 Petrol. 159, 159–174.

562 Ellis, D., Green, D., 1979. An experimental study of the effect of Ca upon garnet-clinopyroxene Fe-Mg
563 exchange equilibria. Contrib. Min. Petrol. 71, 13–22.

564 Fiannacca, P., Lo Po, D., Ortolano, G., Cirrincione, R., Pezzino, A., 2012. Thermodynamic modeling
565 assisted by multivariate statistical image analysis as a tool for unraveling metamorphic P-T-s
566 evolution: an example from ilmenite-garnet-bearing metapelite of the Peloritani Mountains,
567 Southern Italy. Miner. Petrol. 106, 151-171.

568 Friel J.J. and Lyman, 2006. X-ray mapping in electron-beam instruments. Microsc. Microanal. 12, 2-
569 25.

570 Ganguly, J., 1979. Garnet and clinopyroxene solid solutions, and geothermometry based on Fe-Mg
571 distribution coefficient. Geo. Cosmo. Acta. 43(7), 1021–1029.

572 Ganne, J., De Andrade, V., Weinberg, R.F., Vidal, O., Dubacq, B., Kagambega, N., Naba, S.,
573 Baratoux, L., Jessell, M., Allibon, J., 2012. Modern-style plate subduction preserved in the
574 Palaeoproterozoic West African craton. Nature Geoscience 5, 60–65.

575 Goldman, D., Albee, A., 1977. Correlation of Mg/Fe partitioning between garnet and biotite with
576 O_{18}/O_{16} partitioning between quartz and magnetite. Am. J. Sc. 277, 750–761.

577 Graham, C. & Powell, R., 1984. A garnet-hornblende geothermometer: calibration, testing, and
578 application to the Pelona Schist, Southern California. J. Metam. Geol. 2(1), 13–31.

579 Grambling, J.A., 1990. Internally-consistent geothermometry and H_20 barometry in metamorphic
580 rocks: the example garnet-chlorite-quartz. Contrib. Min. Petrol. 105, 617-628.

581 Green, T., Hellman, P., 1982. Fe-Mg partitioning between coexisting garnet and phengite at high
582 pressure, and comments on a garnet-phengite geothermometer. Lithos 15, 253–266.

583 Guillot, S., Riel, N., Hattori, K., Desgreniers, S., Rolland, Y., Van Melle, J., Latif, M., Kausar, A.,
584 Pêcher, A., 2008. New occurence of eclogitic continental rocks in NW Himalaya: The Stak
585 massif in northern Pakistan. Himalayan journal of sciences 5, 57–58.

586 Guillot, S. Hattori, K., Agard, P., Schwartz, S., Vidal, O. (2009) Exhumation processes in oceanic and
587 continental subduction contexts : a review. In S. Lallemand and F. Funiciello (eds.) Subduction
588 Zone Dynamics, 175-204, doi 10.1007/978-3-540-87974-9, Springer-Verlag Berlin Heidelberg.

589 Hammarstrom, J., Zen, E., 1986. Aluminum in hornblende; an empirical igneous geobarometer. Am.
590 Min. 71, 1297–1313.

591 Hillier, S., Velde, B., 1991. Octahedral occupancy and chemical composition of diagenetic (low-
592 temperature) chlorites. Clay Min. 26, 149.

593 Holdaway, M., Lee, S., 1977. Fe-Mg cordierite stability in high-grade pelitic rocks based on
594 experimental theorical and natural observations. Contrib. Min. Petrol. 63, 175–17198.

595 Holland, T., Baker, J., Powell, R., 1998. Mixing properties and activity-composition and relationships
596 of chlorites in the system MgO-FeO-Al 2O3-SiO2-H2O. Eur. J. Min. 10, 395-406.

597 Holland, T., Blundy, J., 1994. Non-ideal interactions in calcic amphiboles and their bearing on
598 amphibole-plagioclase thermometry. Contrib. Min. Petrol. 116, 433–447.

599 Holland, T., Powell, R., 1998. An internally consistent thermodynamic data set for phases of
600 petrological interest. J. Metam. Geol. 16, 309–343.

601 Holland, T., Powell, R., 2011. An improved and extended internally consistent thermodynamic dataset
602 for phases of petrological interest, involving a new equation of state for solids. J. Metam. Geol.
603 29, 333–383.

604 Hollister, L.S., Grissom, G., Peters, E., Stowell, H., Sisson, V., 1987. Confirmation of the empirical
605 correlation of Al in hornblende with pressure of solidification of calc-alkaline plutons. Am.
606 Min. 72, 231.

607 Inoue, A., Meunier, A., Patrier-Mas, P., Rigault, C., Beaufort, D., Vieillard, P., 2009. Application of
608 Chemical Geothermometry to Low-Temperature Trioctahedral Chlorites. Clays and Clay Min.
609 57, 371–382.

610 Joanny, V., van Roermund, H., Lardeaux, J.M., 1991. The clinopyroxene/plagioclase sympelctite in
611 retrograde eclogites: a potential geothermobarometer. Geologische Rundschau 80(2), 303-320.

612 Johnson, M., Rutherford, M., 1989. Experimental calibration of the aluminum-in-hornblende
613 geobarometer with application to Long Valley valdera (California) volcanic rocks. Geology 17,
614 837–841.

615 Jowett, E., 1991. Fitting iron and magnesium into the hydrothermal chlorite geothermometer:
616 GAC/MAC/SEG, Presented at the Joint Annual Meeting (Toronto, May 27-29, 1991) Program
617 with Abstracts.

618 Kawasaki, T., Nakano, N., Osanai, Y., 2011. Osumilite and a spinel+quartz association in garnet–
619 sillimanite gneiss from Rundvågshetta, Lützow-Holm Complex, East Antarctica. Gondwana
620 Research 19, 430–445.

621 Kohn, M.J. and Spear, F., 2000. Retrograde net transfer reaction insurance for pressure-temperature

622 estimates. Geology 28, 1127-1130.

623 Kranidiotis, P., MacLean, W., 1987. Systematics of chlorite alteration at the Phelps Dodge massive
624 sulfide deposit, Matagami, Quebec. Economic Geology and the Bulletin of Society of Economic
625 Geologists 82, 1898–1911.

626 Krogh, E.J., Råheim, A., 1978. Temperature and pressure dependence of Fe-Mg partitioning between
627 garnet and phengite, with particular reference to eclogites. Contrib. Min. Petro. 66, 75–80.

628 Krogh, E.J., 1988. The garnet-clinopyroxene Fe-Mg geothermometer a reinterpretation of existing
629 experimental data. Contrib. Min. Petro. 99(1), 44–48.

630 Lanari, P., Guillot, S., Schwartz, S., Vidal, O., Tricart, P., Riel, N., Beyssac, O., 2012. Diachronous
631 evolution of the alpine continental subduction wedge: Evidence from P–T estimates in the
632 Briançonnais Zone houillère (France – Western Alps). J. Geodynamics 56-57, 39–54.

633 Lanari, P., Riel, N., Guillot, S., Vidal, O., Schwartz, S., Pêcher, A., Hattori, K. (2013). Deciphering
634 High-Pressure metamorphism in collisional context using microprobe-mapping methods:
635 application to the Stak eclogitic massif (NW Himalaya). Geology, 41, 111-114.

636 Launeau, P., Cruden, A.R., and Bouchez, J.L. (1994) Mineral recognition in digital images of rocks: a
637 new approach using multichannel classification. Can. Min. 32, 919–933.

638 Massone, H., Schreyer, W., 1987. Phengite geobarometry based on the limiting assemblage with K-
639 feldspar, phlogopite and quartz. Contrib. Min. Petrol. 96, 212–224.

640 Mori, T. & Green, D., 1978. Laboratory duplication of phase equilibria observed in natural garnet
641 lherzolites. J. Geol. 86, 83–97.

642 Muñoz, M., De Andrade, V., Vidal, O., Lewin, E., Pascarelli, S., Susini, J., 2006. Redox and speciation
643 micromapping using dispersive X-ray absorption spectroscopy: Application to iron in chlorite
644 mineral of a metamorphic rock thin section. Geochem. Geophys. Geosyst. 7(11) 1-10.

645 Mysen, B. and Heier, K., 1972. Petrogenesis of eclogites in high grade metamorphic gneisses,
646 exemplified by the Hareidland eclogite, western Norway. Contrib. Min. Petrol. 36(1), 73–94.

647 Pattison, D. R. M., and Newton, R. C., 1989, Reversed experimental calibration of the garnet-
648 clinopyroxene Fe-Mg exchange thermometer: Contrib. Min. Petrol. 101, 87-103.

649 Parra, T., Vidal, O., Agard, P., 2002. A thermodynamic model for Fe–Mg dioctahedral K white micas
650 using data from phase-equilibrium experiments and natural pelitic assemblages. Contrib. Min.
651 Petrol. 143, 706–732.

652 Perchuk, L., Aranovich, L.Y., Podlesskii, K., Lavrent'eva, I., Gerasimov, V., Fed'kin, V., Kitsul, V.,
653 Karsakov, L., Bernikov, N., 1985. Precambrian granulites of the Aldan shield, eastern Siberia,
654 USSR. J. Metam. Geol. 3, 265–310.

655 Plunder, A., Agard, P., Dubacq, B., Chopin, C., Bellanger, M., 2012. How continuous and precise is
656 the record of P-T paths? Insights from combined thermobarometry and thermodynamic
657 modelling into subduction dynamics (Schistes Lustrés, W. Alps). J. Metam. Geol. 30, 323-346.

658 Powell, R., 1985. Regression diagnostics and robust regression in geothermometer/geobarometer
659 calibration: the garnet-clinopyroxene geothermometer revisited. J. Metam. Geol. 3, 231–243.

660 Powell R. 2008. On thermobarometry. J. Metam. Geol. 26, 155–179.

661 Pourteau, L., Sudo, M., Candan, O., Lanari, P., Vidal, O., Oberhänsli, R. (2013). Neotethys closure
662 history of Anatolia: insights from 40Ar–39Ar geochronology and P–T estimation in high
663 pressure metasedimentary rocks. J. Metam. Geol. doi:10.1111/jmg.12034.

664 Prêt, D., Sammartino, S., Beaufort, D., Meunier A., Fialin, M., Michot, L.J. (2010). A new method for
665 quantitative petrography based on image processing of chemical element maps: Part I. Mineral
666 mapping applied to compacted bentonites. Am. Min. 95, 1379-1388.

667 Råheim, A., Green, D.H., 1974. Experimental determination of the temperature and pressure
668 dependence of the Fe-Mg partition coefficient for coexisting garnet and clinopyroxene. Contrib.
669 Min. Petrol. 48, 179–203.

670 Ravna, E.K., 2000a. The garnet–clinopyroxene Fe2+–Mg geothermometer: an updated calibration. J.
671 Metam. Geol. 18, 211–219.

672 Ravna, E.K., 2000b. Distribution of Fe2+ and Mg between coexisting garnet and hornblende in
673 synthetic and natural systems: an empirical calibration of the garnet-hornblende Fe-Mg
674 geothermometer. Lithos 53, 265–277.

675 Reed, S.J.B. 2005. Electron microprobe analysis and scanning electron microscopy in geology. 2nd
676 edition, Cambridge University Press.

677 Riel, N., Hattori, K., Guillot, S., Rayner, N., Davis, N., Latif, M., Kausar, M., 2008, SHRIMP zircon
678 ages of eclogites in the Stak massif, northern Pakistan: Himalayan Journal of Sciences, 5, 119–
679 120.

680 Saporta, G., 1990. Probabilités, analyse des données et statistique. Editions Technip, Paris.

681 Schmidt, M.W., 1992. Amphibole composition in tonalite as a function of pressure: an experimental
682 calibration of the Al-in-hornblende barometer. Contrib. Min. Petrol. 110, 304–310.

683 Seber, G., 1984. Multivariate Observations. Hoboken, NJ: John Wiley & Sons, Inc.

684 Sengupta, P., Dasgupta, S., Bhattacharya, P. K., and Hariya, Y., 1989, Mixing behavior in quaternary
685 garnet solid solution and an extended Ellis and Green garnet-clinopyroxene geothermometer.
686 Contrib. Min. Petrol. 103, 223-227.

687 Spath, H., 1985. Cluster dissection and analysis: theory, FORTRAN programs, examples. New York:
688 Halsted Press.

689 Spear, F., 1995. Metamorphic phase equilibria and Pressure-Temperature-time paths. Mineral Society
690 of America, Washington.

691 Thompson, A., 1976. Mineral reactions in pelitic rocks: II. Calculation of some P-T-X(Fe-Mg) phase
692 relations. Am. J. Sc. 276, 425–454.

693 Tinkham, D.K., Ghent, E.D., 2005. XRMapAnal: A program for analysis of quantitative X-ray maps.
694 Am. Min. 90, 737-744.

695 Vidal, O., Parra, T., 2000. Exhumation paths of high-pressure metapelites obtained from local
696 equilibria for chlorite–phengite assemblages. Geol. J. 35, 139–161.

697 Vidal, O., Goffé, B., Bousquet, R., Parra, T., 1999. Calibration and testing of an empirical
698 chloritoid–chlorite Mg–Fe exchange thermometer and thermodynamic data for daphnite. J.
699 Metam. Geol. 17, 25–39.

700 Vidal, O., Parra, T., Trotet, F., 2001. A Thermodynamic Model for Fe-Mg Aluminous Chlorite Using
701 Data from Phase Equilibrium Experiments and Natural Pelitic Assemblages in the 100 to 600°C,
702 1 to 25 kb Range. Am. J. Sc. 301, 557.

703 Vidal, O., Parra, T., Vieillard, P., 2005. Thermodynamic properties of the Tschermak solid solution in
704 Fe-chlorite: Application to natural examples and possible role of oxidation. Am. Min. 90, 347–
705 358.

706 Vidal, O., De Andrade, V., Lewin, E., Munoz, M., Parra, T., Pascarelli, S., 2006. P-T-deformation-
707 Fe3+/Fe2+ mapping at the thin section scale and comparison with XANES mapping: application
708 to a garnet-bearing metapelite from the Sambagawa metamorphic belt (Japan). J. Metam. Geol.
709 24, 669–683.

710 Warren, C., Waters, D., 2006. Oxidized eclogites and garnet-blueschists from Oman: P–T path

711 modelling in the NCFMASHO system. J. Metam. Geol. 24, 1–20.

712 Waters, D., 1996. The Garnet-Cpx-Phengite barometer. Recommended calibration and calculation
713 method, updated 1 March 1996. (http:
714 //www.earth.ox.ac.uk/~davewa/research/eclogite/ecbarcal.html 1).

715 Waters, D., 2002. Clinopyroxene-Amphibole-plagioclase symplectites in Norwegian eclogites:
716 microstructures, chemistry and the exhumation P-T path. Mineralogical Society, Winter
717 Conference, Derby.

718 Waters, D., 2003. P-T paths from Cpx-Hbl-Pl symplectites, updated 22 February 2003.
719 http://www.earth.ox.ac.uk/~davewa/research/eclogites/symplectites.html.

720 Waters, D., Martin, H., 1993. Geobarometry in phengite-bearing eclogites. Terra Nova 5, 410–411.

721 Yamato, P., Agard, P., Burov, E., Le Pourhiet, L., Jolivet, L., Tiberi, C., 2007. Burial and exhumation
722 in a subduction wedge: Mutual constraints from thermomechanical modeling and natural P-T-t
723 data (Schistes Lustrés, western Alps). J. Geophys. Res. 112, B07410.

724 Zack, T., Moraes, R., Kronz, A., 2004. Temperature dependence of Zr in rutile: empirical calibration of
725 a rutile thermometer. Contrib. Min. Petrol. 148, 471–488.

726 Zang, W., Fyfe, W., 1995. Chloritization of the hydrothermally altered bedrock at the Igarape Bahia
727 gold deposit, Carajas, Brazil. Mineralium Deposita 30, 30–38.

728

729

730

731 **Figure Caption**

732

733 **Fig. 1:** *XMapTools* v1.5.2 graphic user interface. The displayed image is the raw Al-
734 content map of the sample 'Eclogite' (see text for details) unit: number of recorded
735 counts.

736 **Fig. 2:** *XMapTools* operating diagram, schematizing the structure of the program. All
737 steps marked with a star require user action. Light arrows indicate the way forward,
738 bold-arrows the transition between the different sub-programs (Xray, Quanti, Results,
739 see text), and the dashed arrows the available feedback.

740 **Fig. 3:** Intensity recorded on the map versus oxide weight percent concentrations for
741 Si in the studied sample. Blue crosses show point analyses, lines are regressed
742 calibration curves obtained using the median approach described in text. The
743 precision is given depending on the intensity (% at 2σ) following equation 1 (see
744 text).

745 **Fig. 4:** Results from the *XMapTools Chem2D* module. (A) The clinopyroxene
746 compositions are plotted in a binary diagram Na *vs* Mg. Unit is per formula unit
747 (p.f.u.). The pixels displayed in the map are colored in red. (B) Density map
748 calculated from the binary diagram (see text for details). (C) Map of the analyzed area
749 in which clinopyroxene pixels selected in A are in red and the unselected pixels in
750 blue. Black pixels do not belong to the clinopyroxene mask. Selected Na-rich pixels
751 correspond to 25% of the total clinopyroxene pixels.

752 **Fig. 5:** Results from the *XMapTools TriPlot3D* module. (A) Clinopyroxene
753 compositions plotted in a ternary diagram jadeite-diopside-hedenbergite. Unit is the
754 end-member proportion. The selected pixel groups displayed into a map in C are
755 colored according to their group (blue: group 1, cyan: group 2, yellow: group 3). (B)

Density map calculated from the ternary diagram. (C) Map of the analyzed area, in which the selected groups of clinopyroxene pixels in A are plotted with the same colors as in A.

Fig. 6: Phase masks for the "eclogite" sample (A) computed using the 'normalized' method (see text). The part used to compare the two available methods is marked using a dashed rectangle. (B) Comparison between the "classical" and "normalized" methods with a difference image in which black pixels are the pixels not allocated to the same groups with both methods.

Fig. 7: Na-content of clinopyroxene (including omphacite). The different stages of crystallization (labeled 1 to 4) are discussed in the text.

Fig. 8: Diagrams showing the difference between point analyses composition (standard) and the standardized composition on the same location on the X-ray maps for garnet and different elements. (A) SiO_2, (B) Al_2O_3, (C) FeO, (D) CaO, (E) MgO, (F) MnO, (G) TiO_2, (H) K_2O, (I) Na_2O. *BDL*: below detection limit.

Fig. 9: P-T path and P-T maps of the Stak sample estimated from the compositions of clinopyroxenes (see text for details). The interpreted *P-T* path is from Lanari et al. (2013).

775 **Table captions**

776

777 **Table 1**: List of solid-solution models and associated end-members included in
778 XMapTools.

779 **Table 2:** List of exchange reaction calibrations included in XMapTools.

780 **Table 3:** List of empirical thermometers, barometers and multi-equilibrium functions
781 implemented in XMapTools.

782 **Table 4:** Phase proportions (volume %) estimated with XMapTools using the
783 available methods 'normalized' and 'classical'. The difference in percentage is an
784 absolute difference.

785 **Table 5:** Uncertainties resulting from microprobe acquisition on raw data and error-
786 propagation using Monte-Carlo techniques on quantified data and structural formulae
787 for clinopyroxene. The precision at 2σ-level on raw data (in %) was estimated using
788 the equation 2 (see text) on the average intensity of all the pixels of clinopyroxene.
789 This uncertainty was propagated on the quantification process using a Monte-Carlo
790 simulation with n=100 000 analyses. The uncertainty was similarly propagated on the
791 structural formulae calculation process, including atom-site distribution.

792

Figure 1

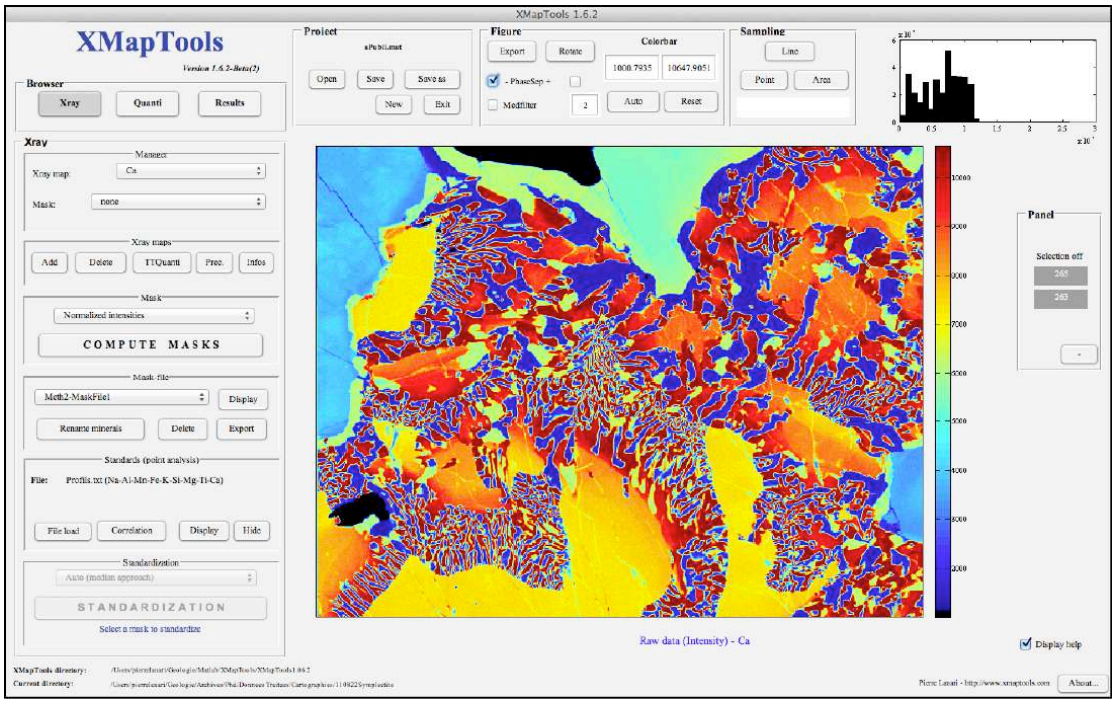

Figure 2

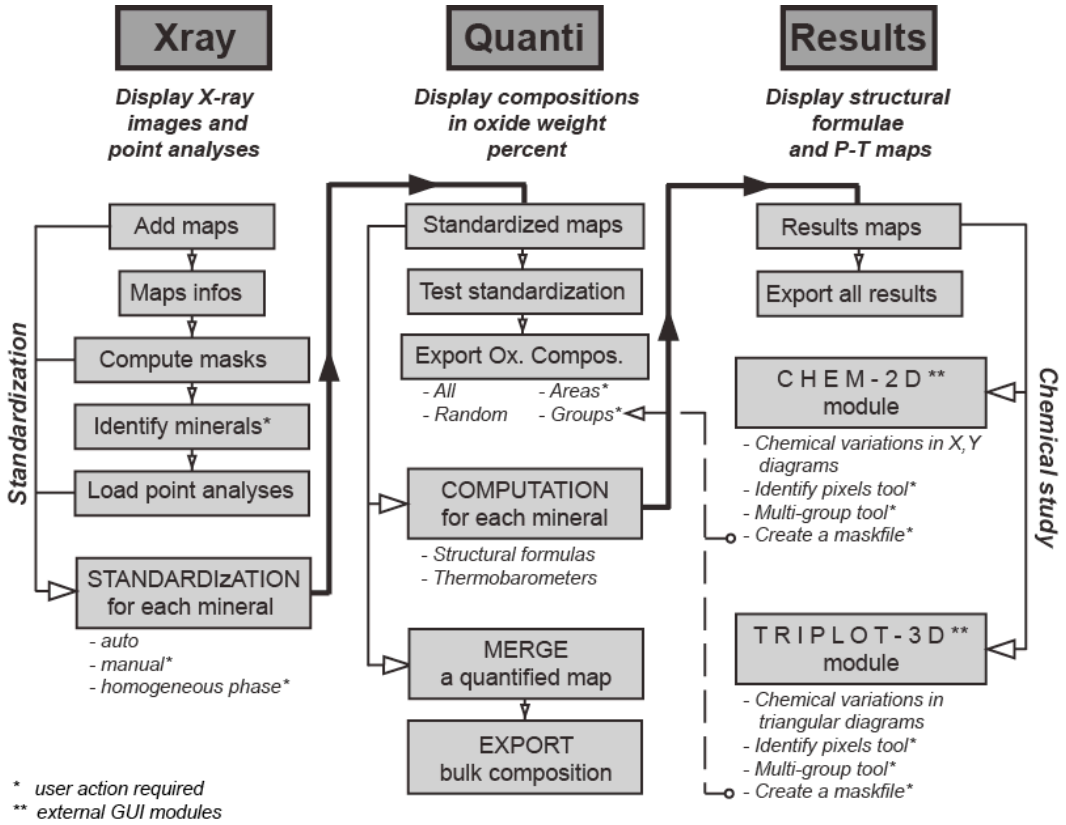

799 **Figure 3**

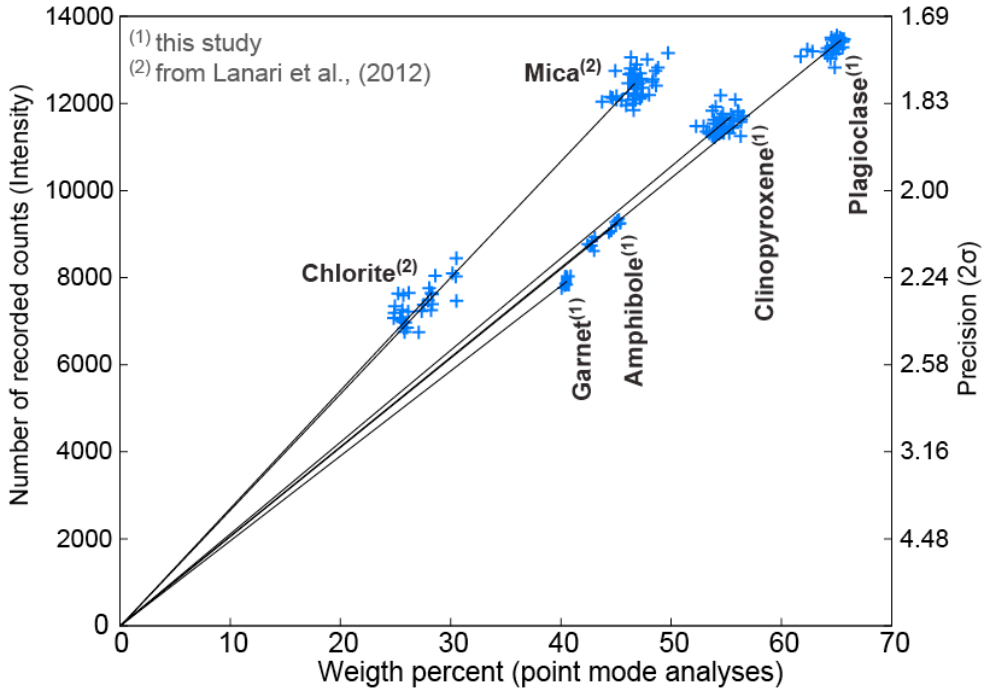

800

801

802

803 **Figure 4**

804

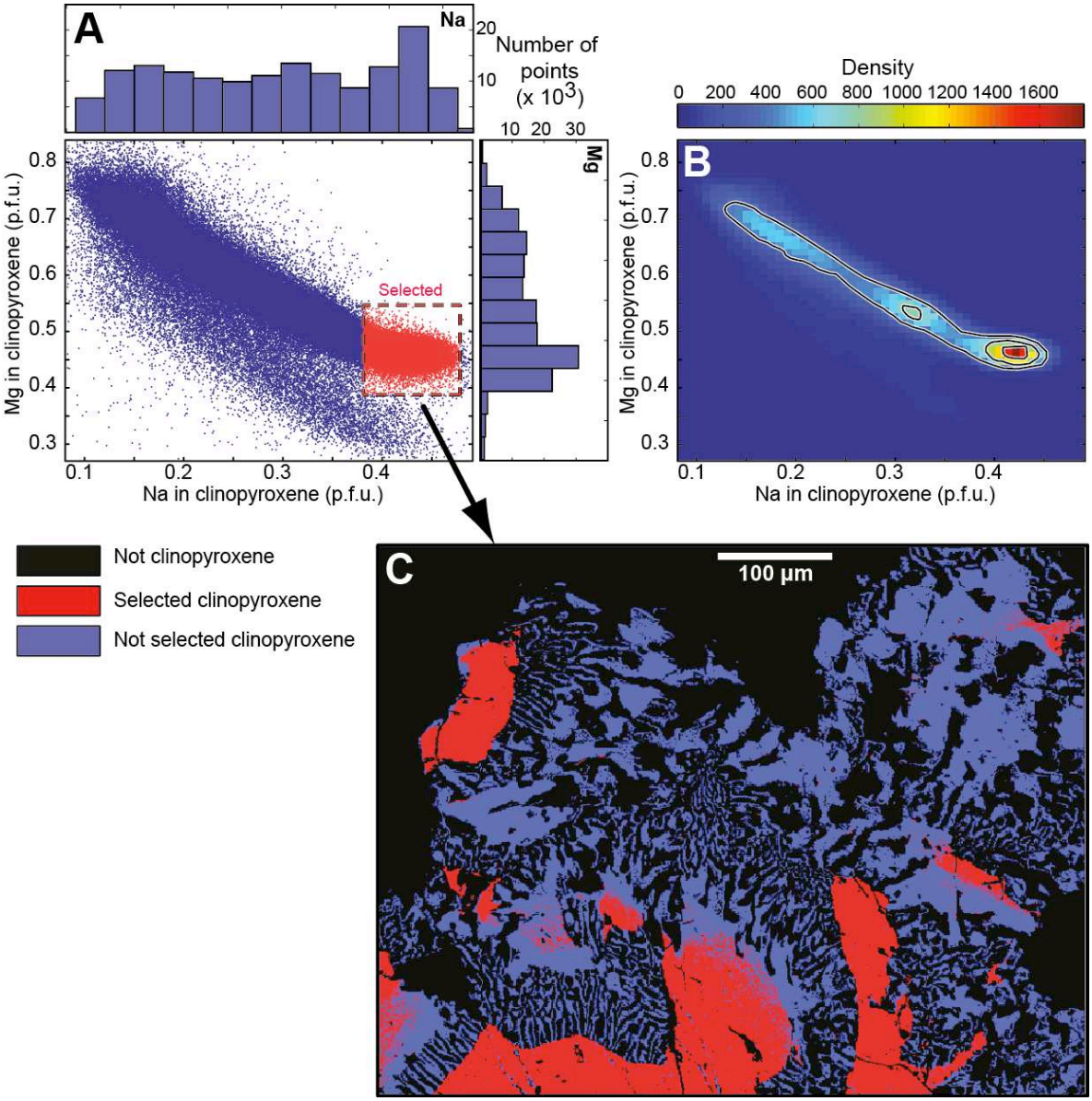

805

806

807 **Figure 5**

808

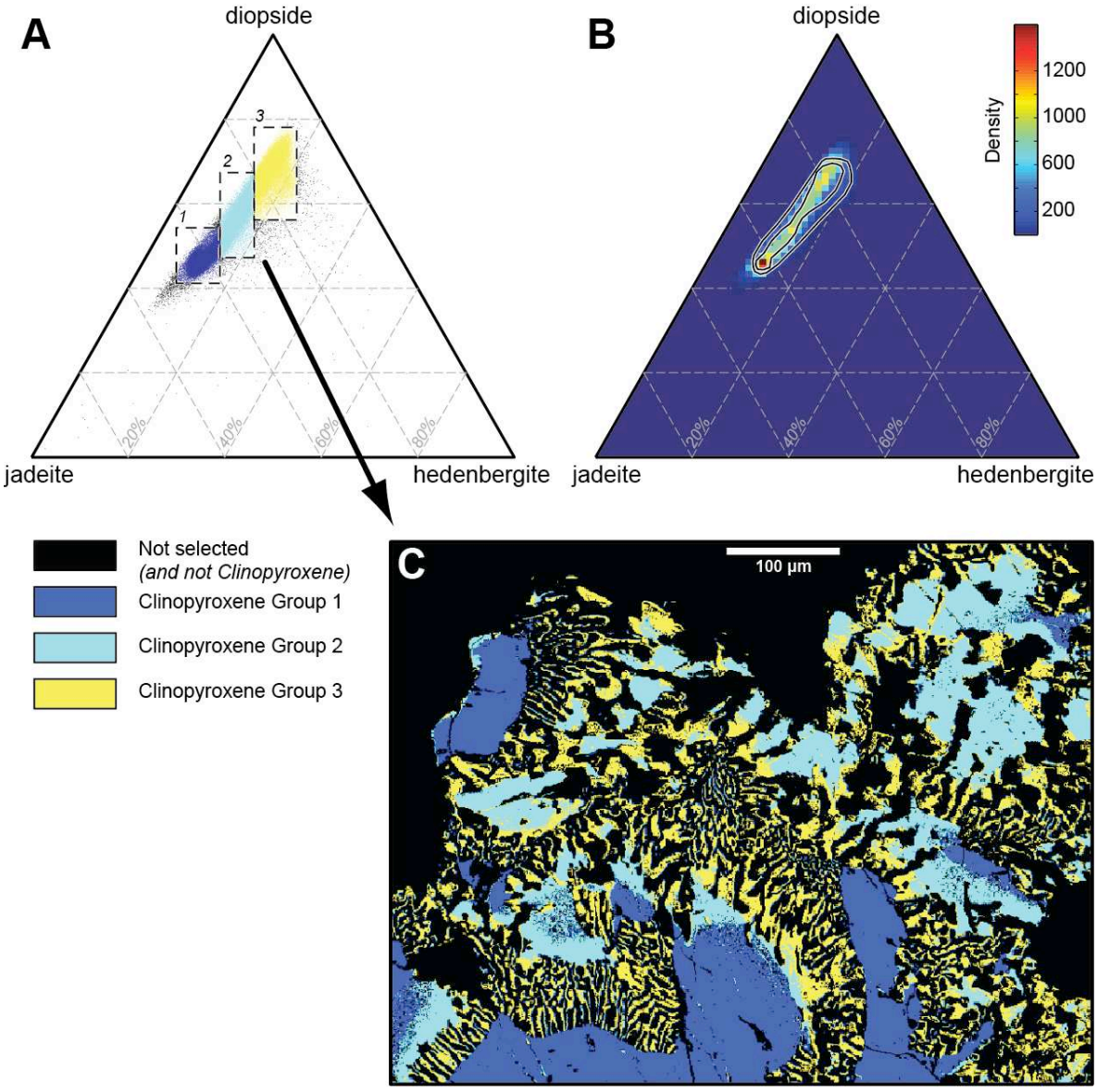

809

810

Figure 6

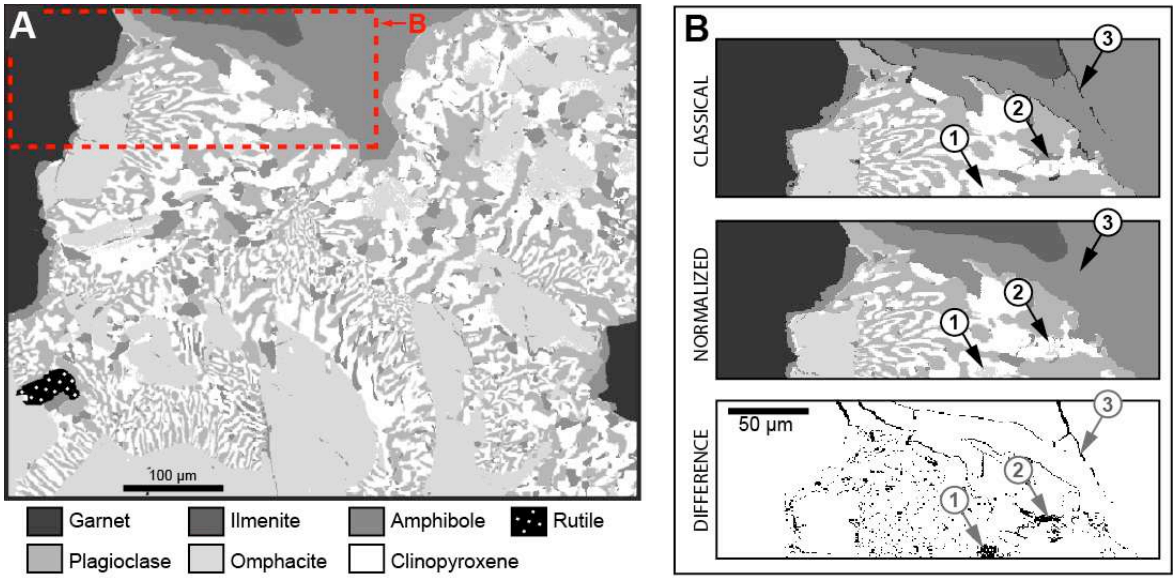

Figure 7

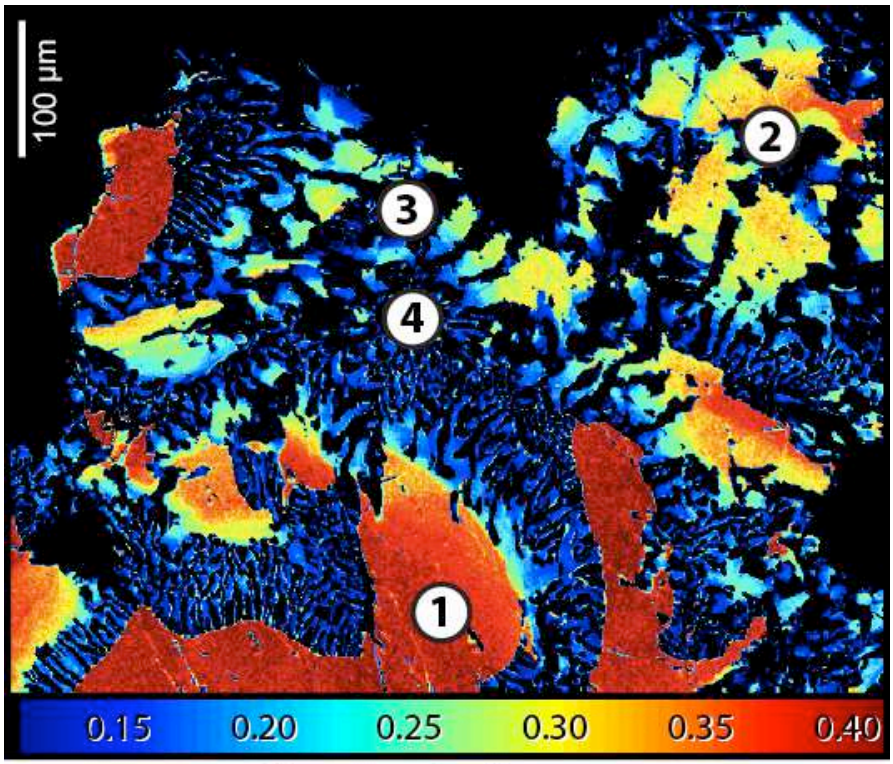

819 **Figure 8**

820

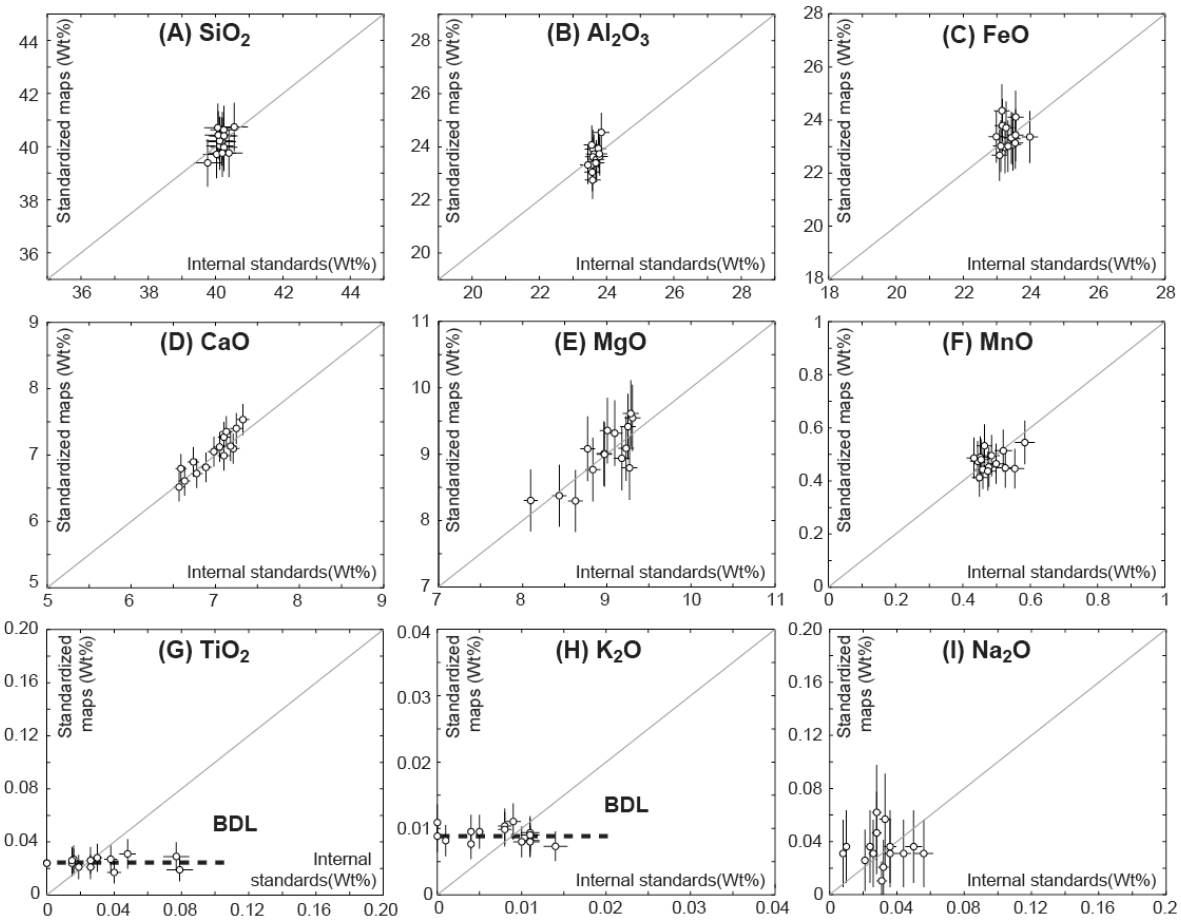

821

822

Figure 9

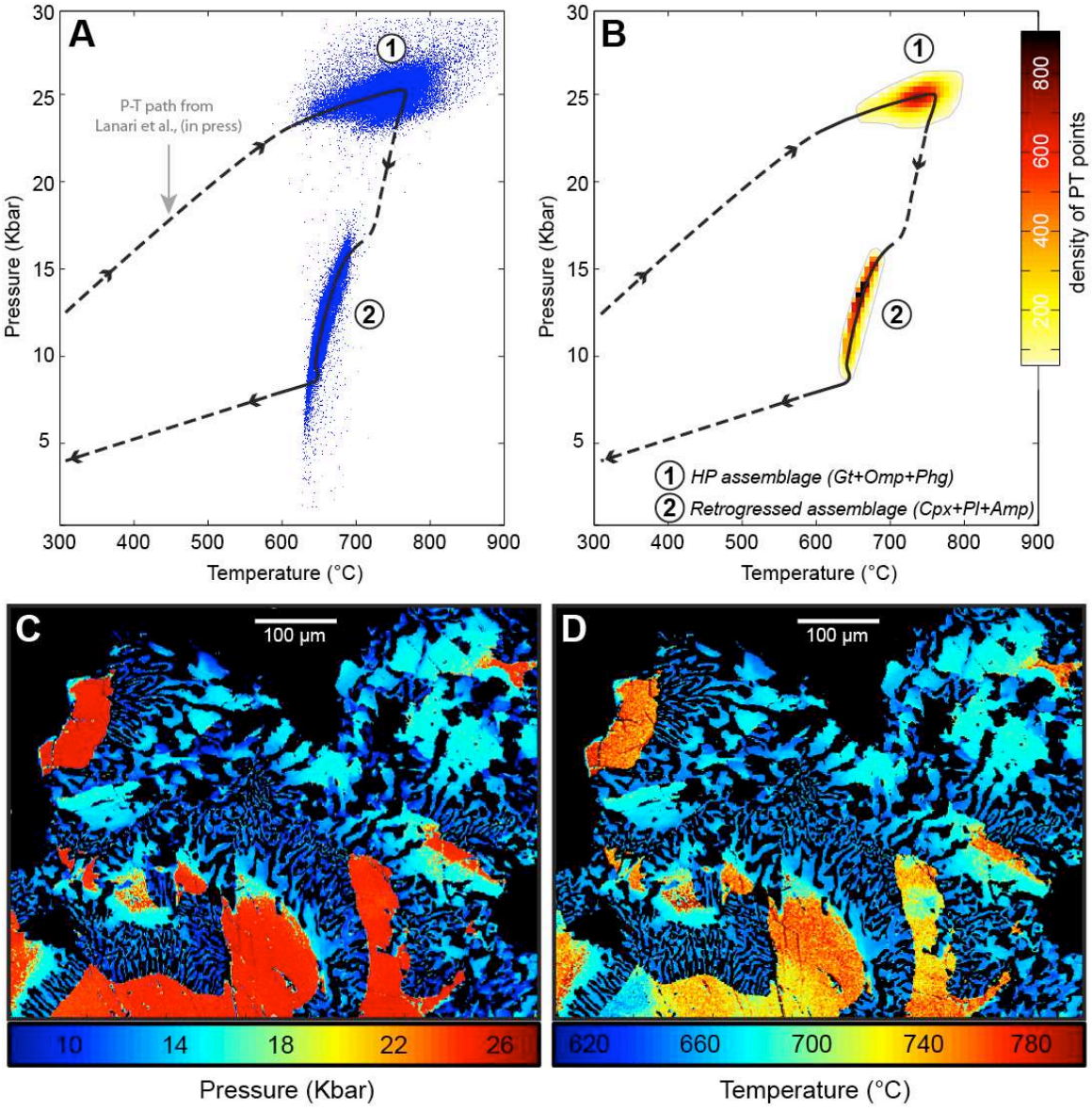
A
B
C
D
P-T path from
Lanari et al., (in press)
Pressure (Kbar)
Temperature (°C)
density of PT points
1 HP assemblage (Gt+Omp+Phg)
2 Retrogressed assemblage (Cpx+Pl+Amp)
100 µm
10 14 18 22 26
Pressure (Kbar)
620 660 700 740 780
Temperature (°C)

827

Table 1

Group	Mineral (*)	End-members (**)	References
Chain silicates	Amphibole (23)	*glaucophane (gl)* *tremolite (tr)* *f-tremolite (ftr)* *tschermakite (ts)* *pargasite (parg)* *cummingtonite (cum)* *ferri-tschermakite (mfets)*	Holland & Blundy, 1994; Dale et al. (2000, 2005); Spear (1995)
	Clinopyroxene (6)	*jadeite (jd)* *diopside (di)* *hedenbergite (hed)* *Ca-tschermak (cats)* *Acmite (acm)*	Spear (1995); Warren and Waters (2006)
	Orthopyroxene (6)	*Enstatite (en)* *Ferrosilite (fs)* *Mg-Tschermak (mgts)*	Holland and Powell (1998)
	Chloritoid (6)	*Fe-chloritoid (fctd)* *Mg-chloritoid (mctd)* *Mn-chloritoid (mnctd)*	Vidal et al. (1999)
	Staurolite (48)	*Fe-staurolite (fst)* *Mg-staurolite (mst)* *Mn-staurolite (mnst)*	Holland and Powell, (1998)
	Epidote (12.5)	*zoizite (zo)* *epidote (ep)* *Fe-epidote (fep)*	Holland and Powell, (1998)
	Cordierite (18)	*cordierite (crd)* *Fe-cordierite (fcrd)* *Mn-cordierite (mncrd)*	Holland and Powell, (1998)
Ortho- & ring silicates	Garnet (12)	*almandine (alm)* *pyrope (pyr)* *spessartine (spe)* *grossular (gro)*	Spear (1995)
	Olivine (4)	*forsterite* *fayalite*	Spear (1995)
Phylosilicates	Chlorite (14)	*amesite (ames)* *f-amesite (fames)* *daphnite (daph)* *sudoite (sud)* *chlorite-Mg (afchl)* *chlorite-Fe (fafchl)*	Holland et al. (1998); Vidal et al. (2001, 2005, 2006)
	Micas (11)	*celadonite (cel)* *f-celadonite (fcel)* *muscovite (mus)* *paragonite (par)* *margarite (marg)* *phlogopite (phl)* *f-phlogopite (fphl)* *pyrophylite (prl)*	Coggon and Holland (2002); Parra et al. (2002); Dubacq et al. (2010)
Framework silicates	Feldspar (8)	*albite (ab)* *anortite (an)* *microcline (mic)*	Spear (1995)

828 * Oxygen basis; ** abbreviation

829

830 **Table 2**

831

Method	Calibrations
Amphibole-Plagioclase	Blundy and Holland (1990); Holland and Blundy (1994)
Chlorite-Chloritoid	Vidal et al. (1999)
Garnet-Biotite	Thompson (1976); Goldman and Albee (1977); Holdaway and Lee (1977)
Garnet-Muscovite	Green and Hellman (1982); Krogh and Râheim (1978)
Garnet-Chlorite	Dickenson and Hewitt (1986); Grambling (1990)
Garnet-Amphibole	Ravna (2000b); Perchuk et al. (1985); Graham and Powell (1984)
Garnet-Cpx	Ravna (2000a); Ai (1994); Sengupta et al. (1989); Pattisson and Newton (1989); Krogh (1988); Powell (1985); Dahl (1980); Ganguly (1979); Ellis and Green (1979); Mori and Green (1978); Râheim and Green (1974); Mysen and Heier (1972)

832

833

834

835 **Table 3**

836

Mineral	Thermometers	Barometers	Multi-equilibrium
Amphibole	T; Holland ans Blundy (1994)	P; Anderson and Smith (1995) P; Schmidt (1992) P; Johnson and Rutherford (1989) P_{min}; Johnson and Rutherford (1989) P_{max}; Johnson and Rutherford (1989) P; Hollister et al. (1987) P; Hammarstrom and Zen (1986)	**Amphibole + plagioclase*** P from Schmidt (1992) and T from Holland and Blundy (1994). **Amphibole + plagioclase* + quartz*** P from Schmidt (1992) and T from Holland and Blundy (1994).
Chlorite	T; Inoue et al. (2009) T; Zang and Fyfe (1995) T; Jowett (1991) T; Hillier and Velde (1991) T; Cathelineau (1988) T; Kranidiotis and MacClean (1987) T; Cathelineau and Nieva (1985)		
Clinopyroxene		P; Waters (2002, 2003)	**Cpx + garnet* + phengite*** P from garnet – omphacite – phengites barometer of Waters and Martin (1993) and Waters (1996) and T from garnet – omphacite thermometer of Ravna (2000a) or Ellis and Green(1979). **Cpx + amphibole* + plagio*** T from amphibole – plagioclase thermometer of Holland and Blundy (1994) and P for the cpx – plagioclase barometer of Waters, (2002, 2003)
K-White mica		P; Massone and Schreyer (1987)	
Garnet	T; Creighton (2009) T; Kawasaki and Motoyoshi, (2011)		
Rutile	T; Zack et al. (2004)		

837 * Fixed composition

838

839

840

841

842 **Table 4**

843

	Normalized	Classical	Difference (%)
Ti-oxide	0.43	0.43	0
Garnet	7.00	7.70	9.09
Fe-Oxide	1.10	1.13	2.65
Amphibole	13.20	12.77	3.37
Plagioclase	21.26	21.52	1.21
Omphacite	30.97	29.88	3.65
Cpx	26.04	26.57	1.99

844

845

846 **Table 5**

847

Raw data

Element	Mean Intensity	Precision (% at 2σ)
Si	11086	0.950
Ti	93	10.35
Al	2529	1.988
Fe	631	3.981
Mg	1381	2.689
Ca	6486	1.242
Na	470	4.609
K	127	8.889

Quantified data

Oxide	Composition	Error (2σ)
SiO2	54.718	0.528
TiO2	0.180	0.018
Al2O3	9.690	0.194
FeO	4.529	0.176
MgO	10.211	0.276
CaO	16.379	0.206
Na2O	4.050	0.188
K2O	0.020	0.002

Structural formula

	Composition	Error (2σ)
Si_T1	1.962	0.010
Al_T1	0.038	0.010
Al_M1	0.371	0.010
Mg_M1	0.546	0.014
Fe_M1	0.136	0.005
Ca_M2	0.629	0.008
Na_M2	0.281	0.013
XMg	0.801	0.008
XFe	0.199	0.008
Xjd	0.281	0.013
Xdi	0.546	0.014
Xhed	0.136	0.005
Xcats	0.019	0.005

848

849

850

Appendix 1

Ca.txt (file)

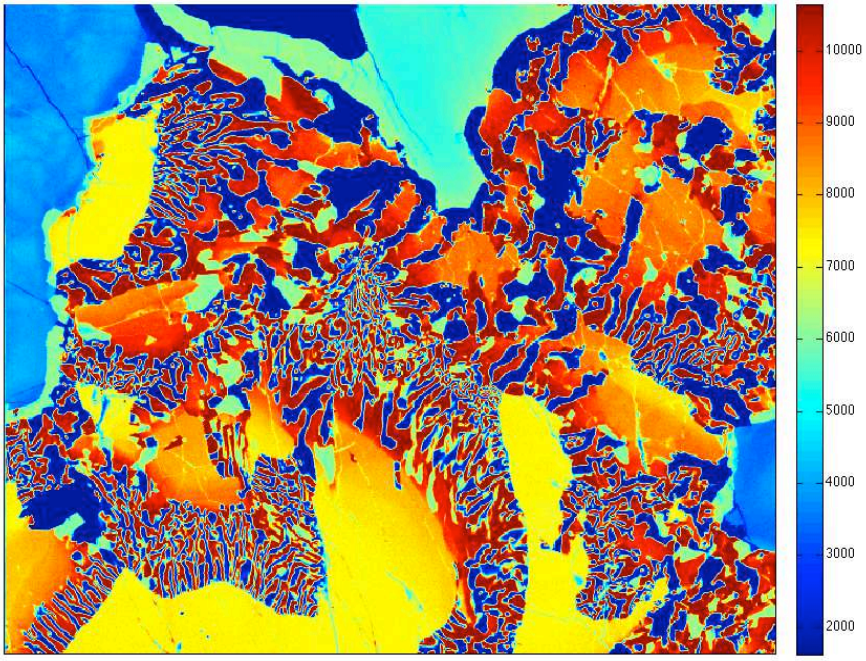

Ca.txt chemical image for the high-pressure Himalayan eclogite sample from the Stak massif in northern Pakistan displayed using XMapTools (unit number of recorded counts, auto-contrast).